Majority Charge Carrier Transport in Particle-Based Photoelectrodes

Yannick K. Gaudy[1], Stefan Dilger[2], Simone Pokrant[3] and Sophia Haussener[1,*]

[1] École Polytechnique Fédérale de Lausanne, Institute of Mechanical Engineering, Laboratory of Renewable Energy Science and Engineering, 1015 Lausanne, Switzerland
[2] Empa Swiss Federal Laboratories for Materials Science and Technology, Laboratory Materials for Energy Conversion, Überlandstrasse 129, 8600 Dübendorf, Switzerland
[3] University of Salzburg, Functional Materials, Jakob-Haringer-Strasse 2a, A-5020 Salzburg, Austria

Abstract

The inter-particle charge transfer of particle-based photoelectrodes was investigated using a particle-based $LaTiO_2N$ photoelectrode as model system. The thickness-dependent front- to back-side illumination photocurrent ratio was measured and compared to the numerical photogenerated current ratio. This comparison suggested the presence of majority charge carrier transport limitations and estimated that only a particle-based film thickness of 450 nm was contributing to the photocurrent. We introduced three different theoretical inter-particle charge transfer mechanisms and implemented their respective equations in a numerical model. The calculated photocurrent-voltage curves were compared to experimental data and proved that inter-particle charge transfer is negligible. Only the particles in direct contact with the fluorine doped tin oxide glass substrate were contributing to the photocurrent. Thus, more efficient particle-based photoelectrodes should incorporate efficient conductive networks connecting particles and substrate. The simulations indicate that the photocurrent density of particle-based photoelectrodes could be increased from 1.2 mA cm^{-2} to 5 mA cm^{-2} at 1.23 V_{RHE} under front-side illumination when adding such a conductive network between particles and substrate.

1. Introduction

The direct conversion of solar energy to hydrogen by using photoelectrochemical (PEC) water splitting approaches has been theoretically calculated to reach up to 40% solar-to-fuel efficiency using a dual bandgap tandem device[1]. Techno-economic calculations indicate that hydrogen produced by photocatalyst particle-suspension devices based on cheap photoabsorbers with a solar-to-fuel efficiency of only 5% can be cost-competitive with hydrogen produced by steam reforming of fossil fuels[2]. However, it has been very challenging to demonstrate experimentally efficiencies even as low as 5%. Experimentally, more successful approaches utilize immobilized photocatalyst particles on conducting substrates, termed particle-based photoelectrodes (PBPE). Such PBPEs are especially interesting as they can be fabricated by low cost dipping procedures, procedures currently used in commercial large-scale battery production[3]. Consequently, PBPEs might show an interesting cost-efficiency tradeoff. PBPEs can use different immobilization approaches, providing a large variety of PE mesostructure designs, which can influence photoabsorption, charge transport, surface charge transfer, independently of the material composition of the individual particles. Moreover, the shape, size, surface area and roughness, and crystallinity of the individual

---

[*] Corresponding author. E-mail address: sophia.haussener@epfl.ch, tel.: +41 21 693 38 78.

particles can be modified, which greatly impact the performance of PBPEs[3]. One important element influencing the performance of PBPE is the inter-particle conductivity. Different approaches have been tested to improve the inter-particle conductivity, for example by adding a, so-called, necking material to connect particles[4] or by adding a carbon containing conductive network linking particles and the conductive substrate[5]. Although the impact of the inter-particle conductivity on the performance of PBPE has been reported[4,6,7], the inter-particle charge transport has never been investigated in details. Nishimura et al. reported a performance increase of PBPEs when applying TiO_2 necking but without attempting to describe or discriminate the inter-particle charge transport [4]. Landsman et al. tried different necking materials such as TiO_2, SnO_2, Ta_2O_5, Nb_2O_5, and Al_2O_3 and observed that PBPEs with TiO_2 necking exhibited the highest photocurrent[3]. Higashi et al. attributed the increase of the photocurrent through necking treatment to the improvement of electron transport between the TaON particles[7]. There was no investigation to determine if the improvement was actually caused by inter-particle conductivity improvement or simply by an improved contact of TaON particles with the fluorine tin doped (FTO) glass substrate. Moreover, a comparison of the photocurrent density under back-side illumination (illuminated from the FTO-side) and front-side illumination (illuminated from the semiconductor-side through the electrolyte) to strengthen or to disprove their hypothesis was missing. Dilger et al.[5] observed that adding a carbon containing conductive network in PBPEs without co-catalysts led to higher front-side illumination photocurrent (front photocurrent) than back-side illumination photocurrent (back photocurrent). They attributed this result to improved majority charge carrier transport, resulting from the added conductive network. Adding co-catalysts inverted the front- to back-side illumination (front to back) photocurrent ratio[8] and was attributed to a limited charge transport capacity of the conductive network for high performing PBPEs[5]. Feng et al.[6] decreased the size of particles in particle-based $LaTiO_2N$ (LTON) PEs in order to increase the active surface area and, thus, the efficiency, as was expected from observations in mesoporous TiO_2 in dye-sensitized solar cells (DSSCs)[9]. Unexpectedly, PBPEs made of smaller particles resulted in lower efficiency. Moreover, the back photocurrent was much higher than the front one for small particles while the illumination side did not influence the performance for larger particles. They attributed this result to the larger number of inter-particle contacts present within the PBPEs made of smaller particles that reduced the electron transport. However, the PBPEs made of larger particles appeared to have only about a single layer of particles and therefore no contribution of upper particles to the photocurrent where observed.

Modeling and theoretical work of particle-based semiconductor substrates such as the mesoporous anatase TiO_2 in DSSCs have been developed over decades. Bisquert and Marcus reviewed the state-of-the-art modeling of DSSCs, which provided insights into the various, coupled transport phenomena occurring in DSSCs and allowed for DSSC's precise characterization[10]. Furthermore, Bisquert developed equivalent-electrical circuits-based transient numerical models to assess the charge transport, generation and recombination behavior of DSSCs. Time constants of charge transfer, trapping, and detrapping were determined by fitting the equivalent circuits to measured impedance spectra of DSSCs[11]. Peter presented the main physico-chemical principles behind DSSCs in order to outline the differences between DSSCs and conventional photovoltaic solar cells. He also analyzed and quantified the different loss mechanisms of DSSCs[12]. In all these modeling and theoretical works, the mesoporous anatase TiO_2 was systematically treated as a low-resistance structure for the transport of electrons where the electron transport follows a diffusion current only. Thus, the mesoporous TiO_2 is neither working as a photoabsorber nor as a material with an internal electric field described by the drift-diffusion current equation. In contrast, the semiconducting particles in PBPEs are photoabsorbers that convert light into electron-hole pairs in

the presence of an electric field (the space charge layer) resulting from the energy level equilibration at the semiconductor-electrolyte interface[13]. Therefore, we cannot treat PBPEs in the same way as mesoporous TiO₂ networks of DSSCs. Particles in PBPE must be treated as photoabsorbers encountering electron-hole pair generation and the charge transport must be described by a drift-diffusion current equation. In our previous work, we developed a numerical model solving the drift-diffusion current equations for holes and electrons to reproduce and predict photocurrent-potential (*I-V*) curves of particle-based LTON PEs[13]. Our model was able to predict the experimental *I-V* curves only when a single layer of particles in contact with the FTO was considered, excluding the contribution to the photocurrent of upper particles. Nevertheless, we did not investigate the reason for this exclusive contribution of the first particle layer to the photocurrent nor the related inter-particle charge transfer.

It becomes obvious from these previous works that the inter-particle charge transfer in PBPEs remains largely unknown and the approach of inter-connecting particles undiscussed. A better understanding is needed to guide research towards high-performing PBPEs. Here, we investigated the inter-particle charge transfer of PBPEs using LTON as model system. First, we experimentally investigated the thickness-dependence and front- and back-side illumination dependence on the photocurrent of the PBPEs in order to provide information about charge transport limitations. The limiting front to back photocurrent ratio depending on the PE's thickness was then computed and compared to the experimental data. This comparison indicated the thickness of the particle-based film that contributes to the photocurrent. Then, we introduced three different theoretical inter-particle charge transfer mechanisms that could describe the inter-particle charge transport of PBPEs. Their related equations were implemented in a numerical model accounting for non-ideal transport behavior and used to calculate *I-V* curves[13]. The numerical *I-V* curves were subsequently compared to experimental *I-V* curves to determine which of the inter-particle charge transfer mechanisms most likely occurred and also if only the particles in direct contact with the FTO were contributing to the photocurrent. In addition, quantification of the potential performance improvements were provided, assuming the different inter-particle charge transfer mechanisms were actually occurring. We finish by discussing the most likely transport between particles and provide design guidance for higher performing PBPEs.

2. Methodology

2.1. Estimated Thickness Contributing to the Photocurrent

The thickness of the LTON PBPEs was controlled by varying the electrophoretic deposition (EPD) time as done by Dilger et al.[5]. The photocurrent density of the PBPEs with different thickness was measured under front and back-side illumination at a potential of 1.23 V vs the reversible hydrogen electrode (V_{RHE}) under the same experimental conditions as Dilger et al.[5]. Bare-LTON electrodes were used for these measurements since adding catalysts would introduce additional effects (section 2.4). The measured thickness-dependent front to back photocurrent ratios of the PBPE were compared to the numerical front to back photogenerated current ratio. The photocurrent is the product of the photogenerated current, i_l, representing the maximum possible current that can be extracted of the photoelectrode (considering realistic absorption behavior and perfect charge transport), and the separation and the injection yields[14,15]:

$$i_{ph} = i_l \times \phi_{sep} \times \phi_{inj}, \tag{1}$$

where the separation yield, ϕ_{sep}, is the yield of photogenerated minority charge carriers reaching the semiconductor-electrolyte interface, and the injection yield, ϕ_{inj}, is the yield of these charges injected into the electrolyte for the water reduction or oxidation reaction. These yields are depending on the charge recombination and transport in the bulk and at the semiconductor-electrolyte interface, but not on the illumination side for holes since they can be extracted orthogonally to the irradiation direction (along the radius of the particle). However, electrons are extracted along the direction of the irradiation. Therefore, the numerical photogenerated current was calculated by integrating the generation rate solved by Beer-Lambert law along the thickness, x_{lim}. x_{lim} is defined as the maximum thickness which still allows electrons to reach the FTO substrate. In other words, x_{lim} corresponds to the thickness of particles contributing to the photogenerated current. Particles below x_{lim} are contributing to the photogenerated current while particles above x_{lim} are not contributing to the photogenerated current. The numerical photogenerated current is given by

$$i_{l,front} = q \int_0^{x_{lim}} \int_0^{\lambda_{gap}} [1 - R_{front}(\lambda)]N(\lambda)e^{-\alpha(\lambda)\rho(d-x)} \, d\lambda dx, \tag{2}$$

under front-side illumination and given by

$$i_{l,back} = q \int_0^{x_{lim}} \int_0^{\lambda_{gap}} [1 - R_{back}(\lambda) - A_{FTO}(\lambda)]N(\lambda)e^{-\alpha(\lambda)\rho x} \, d\lambda dx, \tag{3}$$

under back-side illumination. x is the location through the thickness of the PBPE (along the substrate's surface normal) according to Figure 1, with the FTO-LTON interface corresponding to $x=0$ and the top of the PBPE corresponding to $x=d$. N is the spectral photon flux hitting the PBPE following the global standard spectrum AM1.5G. α is the spectral absorption coefficient of LTON taken from Gaudy et al.[13]. ρ is the solid phase density in the PBPE. The spectral reflectance under front- and back-side illumination, R_{front} and R_{back}, and the absorptance of the FTO glass substrate under back illumination, A_{FTO}, were also taken from Gaudy et al.[13]. For front- and back-side illumination, the absorption in the electrolyte was neglected. The integrals over the wavelength and over the thickness were solved numerically with a resolution of 1 nm. The bandgap wavelength, λ_{gap}, was 590 nm for LTON (bandgap of 2.1 eV).

The front to back photocurrent ratio can be compared to the front to back photogenerated current

$$\frac{i_{ph,front}}{i_{ph,back}} = \frac{i_{l,front} \times \phi_{sep} \times \phi_{inj}}{i_{l,back} \times \phi_{sep} \times \phi_{inj}} = \frac{i_{l,front}}{i_{l,back}}. \tag{4}$$

As previously mentioned, the separation and the injection yields of the holes are the same for both illumination directions. These yields depend on the illumination direction for electrons and are included in the photogenerated current calculations (eqns (2) and (3)). If a x_{lim} provides a numerical front to back photogenerated current ratio that matches the experimental photocurrent ratio, we assume that this x_{lim} is the thickness of the film that contributes to the photocurrent. However, this x_{lim} is only an estimation of the actual thickness of particles contributing to the photocurrent. Indeed, the solid phase density was not measured for each of the PBPE thicknesses but assumed to be constant at 0.28 according to the density profile in the first 4 μm of a 8.43 μm LTON PBPE from Suter et al.[16]. However, the density profile from Suter et al. is not constant and decreases after 4 μm. Thus, the numerical photogenerated current ratio (eqns (2) and (3)) in PBPE is only an

estimation, and so is x_{lim}. A more precise estimation of x_{lim} could incorporate the measured solid phase density for each of the PBPE thicknesses and by calculating the generation rate using an EMW propagation model with the exact morphology of the PBPE.

2.2. Theoretical Inter-Particle Charge Transfer Mechanisms

The charge transfer at the LTON particle-TiO$_2$ necking-FTO substrate interface is briefly introduced, before discussing the inter-particle transfer. We hypothesize that the LTON-TiO$_2$ contact provides a built-in field that promotes the electron transfer because the conduction band level of LTON is -4.2±0.1 V vs vacuum (V$_{vac}$)[17] and the conduction band of TiO$_2$ is -4.8 V$_{vac}$ or -5.1 V$_{vac}$, depending on its crystal structure[18]. The electron charge transfer from TiO$_2$ to FTO follows a charge transfer by tunneling rather than a Schottky barrier since the potential barrier width is only 1 nm[19]. Therefore, electrons can transfer from the LTON to the FTO effectively. Whereas, electrons would transfer by a Schottky barrier from LTON to FTO without the TiO$_2$ necking. The potential barrier width would be too large (25 nm for LTON with a potential barrier of 0.3 V and a doping concentration of 7.4×10^{17} cm^{-3} and a permittivity of 15[13]) to allow electron tunneling and thus would severely impact the performance of LTON PBPE, as observed by Landsmann et al.[3]. The inter-particle interface, LTON-TiO$_2$-LTON, is radically different from the LTON-TiO$_2$-FTO contact since there is no FTO. Here, we discuss this difference by introducing three different models for describing the inter-particle charge transfer mechanism. The first inter-particle charge transfer mechanism case, depicted in Figure 1.c case 1, assumes that the majority charge carriers cannot be transported from one particle to the other. Only the photogenerated electrons of the first layer of particles that are in direct contact with the FTO can be collected. This implies that under front-side illumination any additional particles lying on top of the first layer of particles will hinder the light absorbed by the first layer of particles while under back illumination there is simply no additional gain of adding particles on top of the first layer of particles. The energy band diagram of the inter-particle contact in case 1, as depicted schematically in Figure 1.d, can be compared to a double Schottky barrier present at the grain boundary of polycrystalline semiconductors[20,21]. The surface in contact between the particles is much smaller than the surface between grains in well performing polycrystalline semiconductors. Indeed, the grain sizes and boundaries in well performing polycrystalline Si varies from few millimeters to centimeters, while the size of particles and inter-particle contacts in LTON PBPEs varies from nanometers to micrometers[3,16]. Polycrystalline silicon solar cells are poorly performing when the grains are randomly oriented, as is the case for particles in LTON PBPEs, compared to columnar or dendritic orientation having a single crystalline grain from the top to the bottom of the solar cell[22,23]. In analogy to the transport behavior known from Si grains, case 1 assumes a double Schottky barrier that is too high to allow any majority charge carrier transfer between particles. The boundary between the first and the second particle assumes no charge transfer, given by

$$\boldsymbol{i}_n \cdot \hat{\mathbf{n}} = \boldsymbol{i}_p \cdot \hat{\mathbf{n}} = 0, \tag{5}$$

where $\hat{\mathbf{n}}$ is the normal vector to the surface boundary and $\boldsymbol{i}_n$ and $\boldsymbol{i}_p$ are the electron and hole current density, respectively.

The second inter-particle charge transfer mechanisms case, depicted in Figure 1.c case 2, assumes an ohmic contact between particles with a potential drop due to the contact resistance, V_{IPC}. The energy band diagram of the inter-particle contact in case 2, as schematically depicted in Figure 1.d, is treated as grain boundaries in cauliflower-type structures of hematite photoanodes[24], given by[25]

$$V_{SCR} = V_a - V_{FB} - \sum_i^m V_{IPC,i}, \tag{6}$$

where V_{FB} is the flatband potential, V_{SCR} is the space charge region (SCR) potential (a discrete function) and m is the number of inter-particle contacts. If V_{IPC} is too high, the upper particles do not feel the effect of the applied potential, V_a, and, correspondingly, the upper particles do not contribute to the photocurrent. If the inter-particle contact resistance is of medium magnitude and the upper particles are contributing to the photocurrent, we use eqn (6) to compute the SCR potential depending on the height of the particle. Since the potential V_{IPC} is not known, we assumed a linear SCR potential drop depending on the height, x, given by

$$V_{SCR}(x) = V_a\left(1 - \frac{x}{d}\right). \tag{7}$$

d is the PBPE thickness and equals to 8.43 μm as determined in Gaudy et al.[13]. In this case, we assumed a continuous quasi-Fermi level over the height of the PBPE since this model is only driven by the SCR potential drop along every inter-particle contact. In a perfect inter-particle contact, V_{IPC} is negligible. In this case, we tested different situations: i) one for which the effective electron mobility is not influenced by any inter-particles contacts ($\mu_{eff,n} = \mu_{b,n}$), ii) one for which the mobility drops over the height of the PBPE (see eqns (8) and (9)), and iii) one for which the mobility completely drops after the first particle in contact with the FTO. We treated the electron mobility drop over the height in analogy to polycrystalline silicon[26] or mesoporous TiO_2 in DSSC[27], given by

$$1/\mu_{eff,n} = 1/\mu_{b,n} + \sum_i^m 1/\mu_{IPC,n,i}, \tag{8}$$

where $\mu_{eff,n}$ is the effective electron mobility, $\mu_{b,n}$ is the bulk electron mobility, and $\mu_{IPC,n}$ is the inter-particle electron mobility. Since $\mu_{IPC,n}$ is not known, two different mobility drops vs height were assumed. The mobility drop type I of situation ii) is given by

$$\mu_{eff,n}(x) = \mu_{b,n}\left(1 - \frac{x}{d}\right), \tag{9}$$

and the mobility drop type II of situation ii) is given by

$$\mu_{eff,n}(x) = \mu_{b,n}\left(1 - \frac{2x}{d}\right) \text{ for } x \le \frac{d}{2} \text{ and } \mu_{eff,n} = 0 \text{ for } x > \frac{d}{2}, \tag{10}$$

where $\mu_{b,n}$ is 46 cm^2 V^{-1} s^{-1}[13]. The situation iii) of case 2 with a complete drop of mobility results in electrons of upper particles that cannot travel to the FTO glass substrate and leads to the same situation as case 1 (first layer of particle only contributing to the photocurrent).
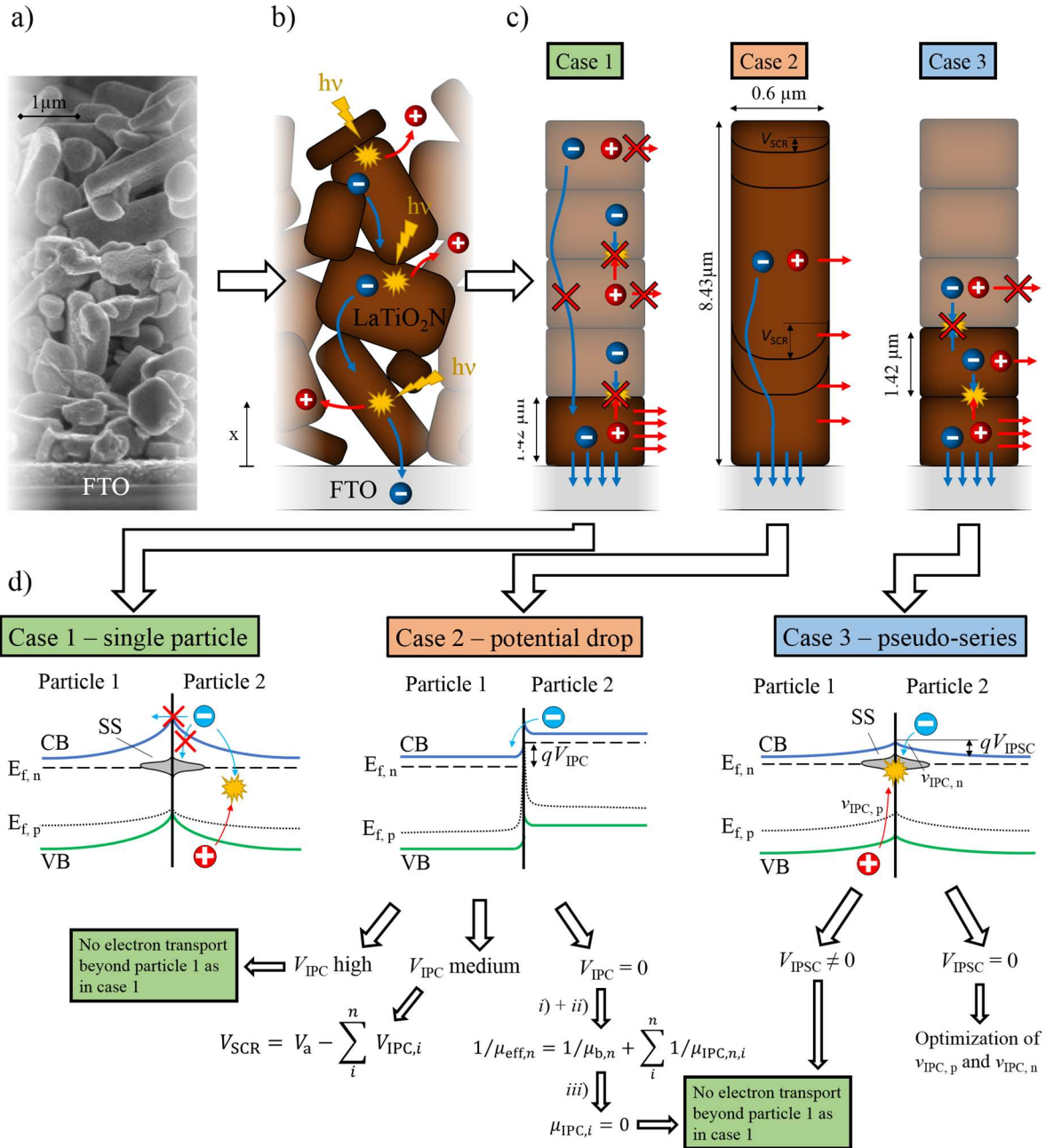
Figure 1. a) SEM of LTON PBPEs, b) schematic of electron and hole generation and transport in LTON particles, c) simplified morphology model considering case 1: only the first layer of particles contributes to the photocurrent, case 2: quasi-Fermi level continuity between the particles, and case 3: particles in "pseudo-series" with computational domain dimensions. d) Details about each case with a scheme of the corresponding energy band diagram.

The third inter-particle charge transfer mechanism case, depicted in Figure 1.c case 3), considers particles in *pseudo-series* with holes and electrons recombining at each inter-particle contact. The term *pseudo-series* is used because every particle is surrounded by the same electrolyte while the contact between particles is in series. In this case, the inter-particle contact is modeled as a Schottky contact with negligible tunneling pinned to an inter-particle contact energy level. The electron and hole current densities are given by

$$i_p \cdot \hat{\mathbf{n}} = q v_{\mathrm{IPC},p}(p_{\mathrm{IPC}} - p_{\mathrm{IPC,eq}}), \tag{11}$$

$$i_n \cdot \hat{\mathbf{n}} = q v_{\mathrm{IPC},n}(n_{\mathrm{IPC}} - n_{\mathrm{IPC,eq}}), \tag{12}$$

where $v_{\mathrm{IPC},p}$ and $v_{\mathrm{IPC},n}$ are the hole and electron inter-particle charge transfer velocities, respectively. p_{IPC} and n_{IPC} are the hole and electron concentrations at the inter-particle contact. $p_{\mathrm{IPC,eq}}$ and $n_{\mathrm{IPC,eq}}$ are the hole and electron concentrations at thermodynamic equilibrium[25]. As depicted in Figure 1.c case 3), this charge transfer mechanism requires that the inter-particle SCL potential, V_{IPSC}, is sufficiently low to have electrons able to reach the inter-particle contact. If V_{IPSC} is too high, the charge transport is suppressed and situation is similar as in case 1 where only the first layer of particles contributes to the photocurrent. If tunneling at the inter-particle contact is high, the inter-particle charge transfer becomes similar to case 2.

This third inter-particle charge transfer mechanism case requires a perfect balance between photogenerated holes from the first particle and photogenerated electrons from the second particle at the inter-particle contact to recombine together. If there is only one type of charge carriers at the interface, this charge transfer mechanism cannot occur. The presence of the electric field in the SCR pushes electron away from the semiconductor-electrolyte (SC-EL) interface while attracting holes. For example the concentration of electrons is five times lower than the one of holes at the SC-EL interface in GaN photoanodes[25]. Thus, mostly electrons are present at the inter-particle contacts and holes at the SC-EL interface. However, the first layer of particles is not only in contact with particles but also with the TiO_2 necking-FTO substrate. In this case, electrons are pushed to the FTO substrate, as previously described, while holes are attracted to the SC-EL interface and to the inter-particle contact (if the electric field is favorable or if there is no electric field by diffusion transport). Moreover, holes at the inter-particle contact in the first particle recombine with electrons from the second particle. Therefore, it is a reasonable assumption that the third layer of particles as well as upper layers do not contribute to the photocurrent since mostly electrons will be present at their inter-particle contacts and holes at the SC-EL interface. Under these conditions, the charge transfer mechanism case 3 implies that the photocurrent remains limited to the photogenerated current in the first layer of particles and that the only benefit of this mechanism is to distribute the photocurrent within the first and second layer of particles.

2.2.1. Computational Photoelectrode Performance Model

The three different inter-particle charge transfer mechanisms cases were implemented in the computational photoelectrode model of Gaudy et al.[13], a 2-dimensional (2D), steady-state multi-physical continuum model that combines electromagnetic wave (EMW) propagation model, charge transfer at the SC-EL interface, charge transport and conservation under steady-state for best-LTON PBPE. The EMW model considered a layer of 2 mm of electrolyte, 8.43 μm of LTON particles with a solid phase density profile taken from Gaudy et al., 360 nm of SnO_2, 2.2 mm of glass, and again 2 mm of electrolyte. The domain sizes of the charge transport and conservation model were approximated by rectangular model domains 1.42 x 0.6 μm for case 1, 8.43 x 0.6 μm for case 2, and (2x1.42) x 0.6 μm for case 3 (see Figure 1). An ohmic contact with thermodynamic equilibrium is present as the bottom boundary for all cases. The SC-EL interfaces were modeled by an adapted Schottky contact[25]. For case 1, SC-EL interfaces are present only on both side boundaries and the top boundary is assumed electronically insulated, i.e. no charge transfer occurred. For case 2, SC-EL interfaces are present on both sides and at the top of the domain's

8

boundary. For case 3, SC-EL interfaces are present at the side boundaries of both particles and the inter-particle contact between the first and the second particle is modeled by a double Schottky contact given by eqns (11) and (12). The top boundary of the second particle is assumed to be insulated (without any charge transfer). The same interfacial hole transfer velocity at the SC-EL interface of 3.5×10^{-6} cm s^{-1} is assumed for all three cases[13]. All the related equations, material parameters, numerical domain sizes, convergence criteria, and mesh discretization of best-LTON PBPE are presented in Gaudy et al.[13].

2.3.   Expected Impact of Particle Size on the Photocurrent

The impact of the particle size on the front to back photocurrent ratio is correlated to the majority charge transfer limitation in PBPEs. If only the first layer of particles in direct contact with the FTO substrate is contributing to the photocurrent, we should observe a decrease of the photocurrent with smaller particle sizes. Moreover, the front photocurrent should be more strongly reduced than the back photocurrent and lead to a smaller front to back photocurrent ratio. However, if the entire film thickness is contributing to the photocurrent, the size of particles should neither impact the photocurrent nor the front to back photocurrent ratio. The impact of particle size on the photocurrent in PBPEs is discussed in section 3.3 using published experimental studies of PBPEs with different LTON particle sizes[6,16,28].

2.4.   Photoelectrode Preparation and Characterization

The LTON particles in this work were synthesized by a solid-state reaction, named SS-LTON[3]. Two types of LTON PBPEs were prepared: the so-called best-LTON with multiple coating process and photocurrent density up to 1.2 mA cm^{-2} at 1.23 V$_{RHE}$ under standard irradiance AM1.5G, and the so-called bare-LTON with a single dipping procedure and lower photocurrent density (ca. 0.1 mA cm^{-2} at 1.23 V$_{RHE}$). The fabrication of both configurations is described in Gaudy et al.[13] and Landsmann et al.[29].

Electrochemical experiments were conducted in a three-electrode setup to refer the potential of our measurements to the RHE. The reference electrode was Ag/AgCl (sat. KCl) and the counter electrode was Pt. The aqueous electrolyte solution was 0.1 M Na$_2$SO$_4$ as a buffer solution with pH=13.2±0.2 by adding NaOH. The sample was illuminated by a solar simulator corresponding to the spectral irradiance of the AM1.5G spectrum. The PBPE's photocurrent thickness dependency was investigated by preparing different electrodes with varying EPD times (i.e. 30, 60, 120, 180, and 240 s), only for bare-LTON PBPEs. Adding catalysts would have added additional effects affecting the photocurrent thickness dependency measurements. The PE thickness was determined by taking the average thickness measured by profilometry. Measurements were done for one sample and current densities are averaged between forward and backward sweeps.

The photocurrent density at 1.23 V$_{RHE}$ was taken as reference value on the forward linear sweep voltammograms. The experimental *I-V* curves of best-LTON PBPEs used in this work were taken from Gaudy et al.[13]. These results were obtained by averaging forward and backward sweeps of eight samples.

3. Results and Discussion

3.1. Thickness Dependency of the Front and Back Photocurrent

We expect the following thickness-dependent photocurrent response for the PBPEs. A poor majority charge carrier transport in PBPEs should lead to an optimum thickness under front-side illumination. At low thicknesses, the photocurrent increases with increasing thickness because photoabsorption is dominating, i.e. thicker films absorb more light. Above a certain thickness, the poor majority charge carrier transport is starting to limit and the photocurrent starts to decrease. An optimum thickness is observed under front-side illumination for photoelectrodes independent of the presence of SCR such as in Cu_2O photocathodes with a SCR[30] or $BiVO_4$ photoanodes without a SCR[31] (purely diffusive charge carrier transport). If no optimum thickness is observed under front-side illumination and the photocurrent is only increasing with the thickness until it reaches a plateau, we can conclude that the majority charge carrier transport is not a limiting factor. If no optimum thickness is observed and the photocurrent is only decreasing, the majority charge carrier transport is limiting but the optimum thickness is below the range of investigated thicknesses. Under back-side illumination, the photocurrent increases limited by absorption. Above a certain thickness, the photocurrent reaches a plateau limited by majority carrier transport, i.e. the upper region is not contributing to the photocurrent anymore.
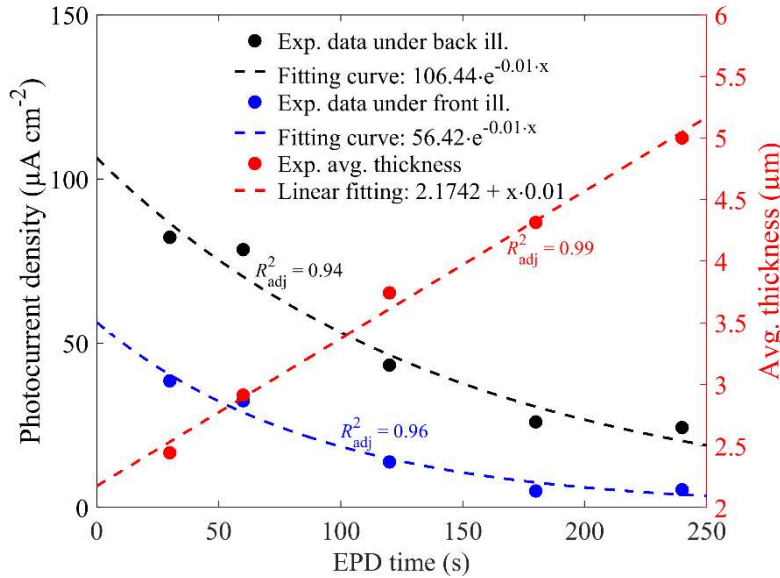

Figure 2. Experimental front- and back-side illumination photocurrent densities at 1.23 V_{RHE} and averaged thicknesses of the PBPE depending on the electrophoretic deposition time for bare-LTON PBPEs. Dashed curves indicate the numerical fit curves with their corresponding goodness of fit (R^2).

In the case of PBPEs, a decrease of the photocurrent with the thickness can be caused either by a poor majority charge carrier transport in the bulk or by a poor inter-particle majority charge carrier transport. Moreover, the thickness cannot be below a single layer of particles, a thickness of 1.42 μm for LTON PBPE, because the particle-based film becomes highly inhomogeneous[5]. As depicted in Figure 2, no optimum thickness was found for experimental front or back photocurrents of bare-LTON PBPEs. Indeed, the photocurrent decreased with increasing thickness under both illumination conditions (front and back). The decrease for front illumination is consistent with the

explanation of strong majority carrier transport limitations. We attribute the progressive decrease of the photocurrent with increasing PBPE thickness under back illumination sides to a reduced amount of necking material at the LTON-FTO contacts with thicker films. We hypothesize that the amount of TiO_2 necking is more distributed over the entire film for thicker films and more concentrated at the FTO-LTON contacts for thinner films. Thus, the photocurrent in thicker films is reduced compared to thinner films. This necking inhomogeneity also affects the front illumination current and, together with the majority current transport limitation, leads to its strong decrease with thickness.

The numerical generation rates (obtained by Beer-Lambert law) and photogenerated current densities (obtained by integrating the generation rates, eqns (2) and (3)) under front- and back-side illumination for case 1 and case 2 are depicted in Figure 3. Case 1, with only the first layer of particles contributing to the photogenerated current (x_{lim}=1.42 µm), is depicted in Figure 3 in opaque colors. Case 2, with the entire particulate film thickness contributing to the photogenerated current is depicted in Figure 3 with semitransparent colors. The front to back photogenerated current ratio is 0.26 for case 1 and 1.11 for case 2 for the thickest PBPE of 5 µm.
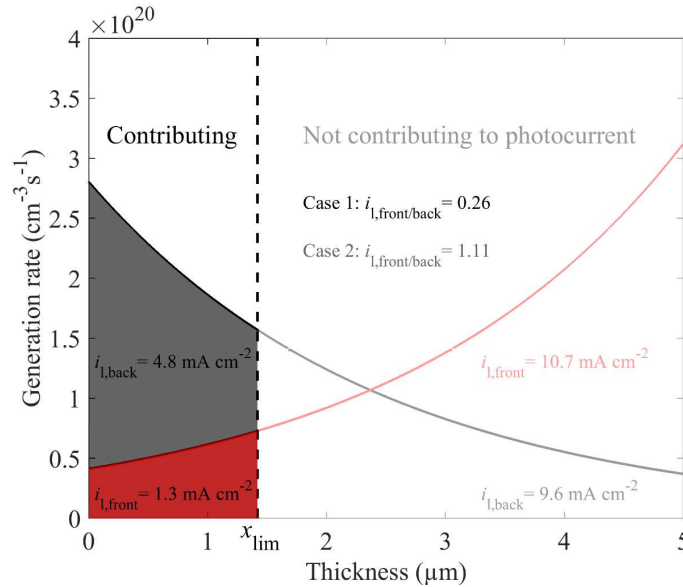

Figure 3. Thickness-dependent generation rate and photogenerated current of a LTON PBPE with a thickness of 5 µm, calculated by eqns (2) and (3) (Beer-Lambert law). The opaque colors are for case 1 considering a single layer of particles (1.42 µm) contributing to the photogenerated current (Figure 1). The semitransparent colors are for case 2 with the full thickness of the PBPE (5 µm) contributing to the photogenerated current (Figure 1). Red color indicates front-side illumination and black color back-side illumination.

The thickness-dependent front to back numerical photogenerated current ratios of cases 1 to 3 are depicted in Figure 4 along with the experimental front to back photocurrent ratio. The numerical photogenerated current ratio of case 1 follows an asymptotic decrease, $1.97 \cdot e^{-0.405 \cdot d}$ (R^2=1), similar to the experimental photocurrent ratio decrease, $1.13 \cdot e^{-0.352 \cdot d}$ (R^2=0.91). The numerical asymptotical decrease, e^{-x}, is caused by the generation rate that follows a Beer-Lambert law, as presented in eqns (2) and (3). For case 2 with the entire film thickness contributing to the photocurrent, the photogenerated current ratio is constant at 1.11 over the thickness. The ratio is higher than one because the FTO glass substrate absorbs some light under back-side illumination and none under front-side illumination (eqns (2) and (3)). Case 3 also shows a front to back

11

photogenerated current ratio with an asymptotic decrease, although the ratio is above one for film thickness below 3 μm. By optimizing the fitting of the numerical photogenerated current ratio to the experimental photocurrent ratio, the contributing thickness, x_{lim}, was found to be 450 nm, smaller than a single layer of particles. Only case 1 with $x_{lim}=1.42$ μm or $x_{lim}=450$ nm exhibit a similar thickness-dependence as the experimental photocurrent ratio. Cases 2 shows a fundamentally different behavior than the experiment. Case 3 shows a similar thickness dependence, however at larger ratios.

The experimental data and numerical case 1 show a stronger decrease of the photogenerated current under front-side illumination ($i_{l,front}/i_{l,back} < 1$), in accordance with an explanation that particles close to the FTO contribute more or exclusively to the photocurrent. Photogenerated current ratios greater than 1, as observed for our case 2, is similar to particles directly connected to the FTO. Such a situation was experimentally measured for LTON PBPE with a network of carbon nanotubes (CNTs) [5], showing a ratio greater than 1 as predicted by our numerical model.

The contributing thickness is calculated to be 450 nm with a solid phase density of 0.28, based on the best fit between the experimental photocurrent ratio and the numerical photogenerated ratio. However, this thickness is only an estimation as explained in 2.1 and thus provides some uncertainty in concluding that exclusively particles in direct contact with FTO are contributing to the photocurrent. However, we claim that the contribution of the upper particles to the photocurrent are most likely negligible as the front to back photogenerated current ratio of case 3 is in disagreement with the experimental data (experimental ratio of 0.47 at 2.5 μm and numerical ratio of 1.15 for case 3 at 2.5 μm) or do not follow the same thickness-dependence (case 2). The solid phase density was assumed constant at 0.28. However, lowering the solid phase density (<0.28) would reduce the absorption coefficient and would result in a thinner contributing thickness (<450 nm). In contrast, increasing the solid phase density would result in a thicker contributing thickness (>450 nm).
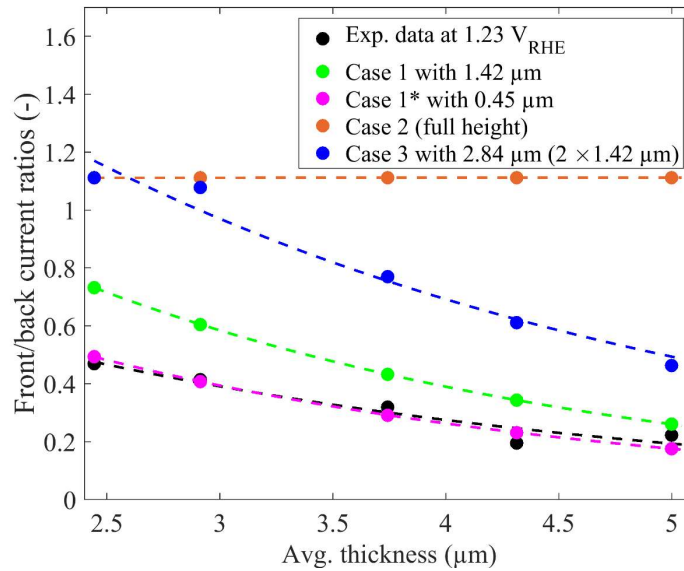

Figure 4. Experimental photocurrent ratio at 1.23 V_{RHE} and numerical photogenerated current ratiodepending on the total averaged thickness of bare-LTON PBPEs. The fitting exponential curves are depicted with dashed lines. The fitting curve for the experimental ratio is given by $1.13 \cdot e^{-0.352 \cdot d}$ ($R^2=0.91$). Case 1, with a current-contributing thickness of 1.42 μm out of the total averaged thickness, has a fitting curve given by $1.97 \cdot e^{-0.405 \cdot d}$ ($R^2=1$). Case 1, with only a current-contributing thickness of 0.45 μm, has a fitting curve given by $1.32 \cdot e^{-0.403 \cdot d}$ ($R^2=1$). Case 2, with the full height contributing to the photogenerated current, has a constant fitting curve of 1.11 ($R^2=1$). Case 3, with only a contributing thickness of 2.82 μm (two times an averaged particle height), has a fitting curve given by $2.67 \cdot e^{-0.338 \cdot d}$ ($R^2=0.95$).

3.2.   Numerical Inter-Particle Charge Transfer Mechanisms

We estimated in the previous section—supported by experimental results as well as numerical results based on photogenerated current model—that the active thickness in LTON PBPEs contributing to the photocurrent is likely equal or even below the thickness of the first layer of particles. In order to provide more support for this conclusion, we show results of the more realistic 2D multi-physics PBPE model incorporating the majority carrier transport and the inter-particle transport mechanisms.
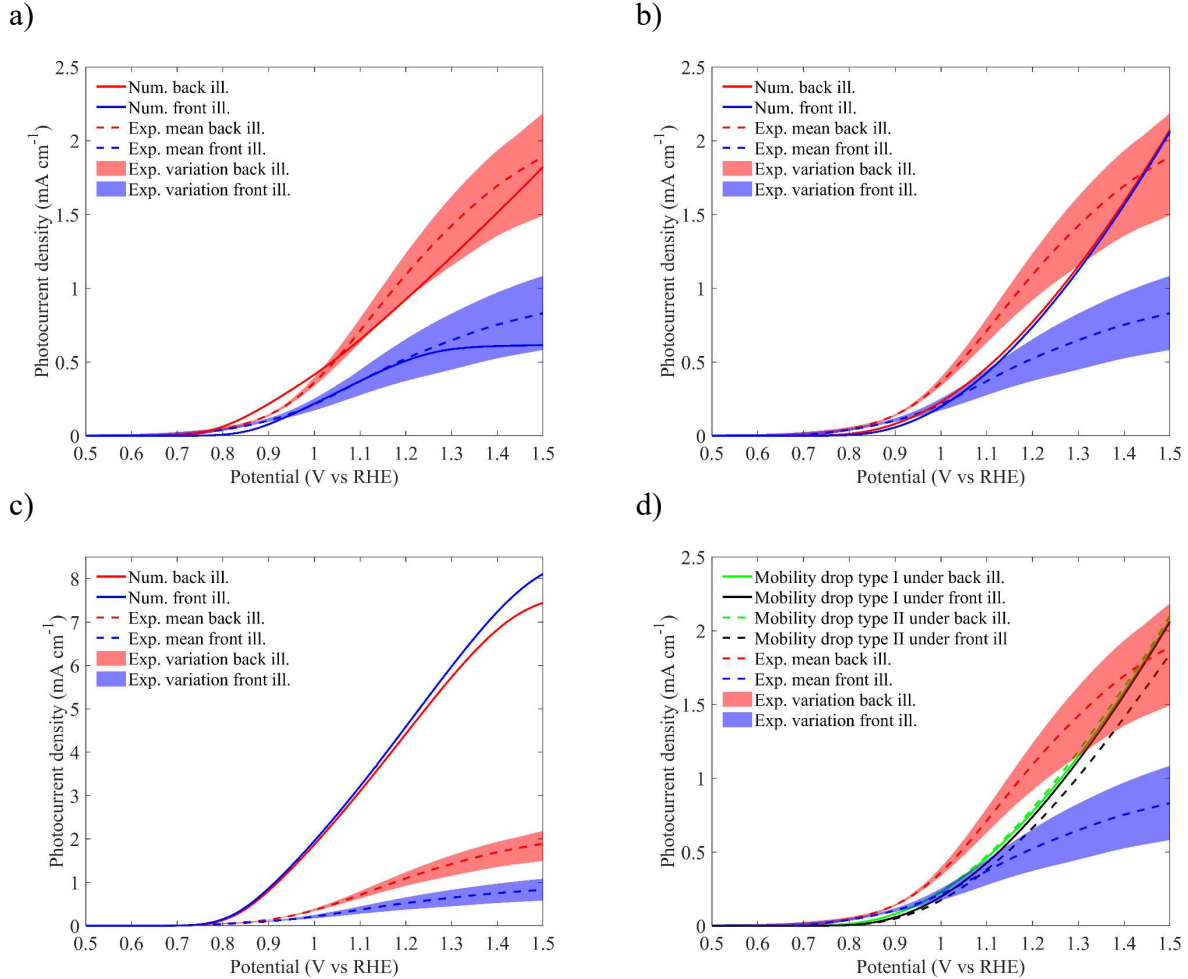
a)

b)

c)

d)

Figure 5. Experimental *I-V* curves of best-LTON PBPEs with an average film thickness of 8.43 μm taken from Gaudy et al.[13]. The corresponding numerical *I-V* curves obtained with the advanced 2D multi-physics PBPE model with assumed inter-particle charge transfer of a) case 1, b) case 2 with linear potential drop and infinite inter-particle mobility (situation *i*), c) case 2 without potential drop and infinite inter-particle mobility (situation *ii*), and d) case 2 without potential drop but mobility drops (type I and II).

The front and back *I-V* curves of case 1 (double Schottky contact with an impassable potential barrier for charge carriers) are depicted in Figure 5.a. The numerical *I-V* curves are within the experimental *I-V* curves variation under front- and back-side illumination. The front and back *I-V* curves of case 2 (potential drop at each inter-particle contacts) with a linear potential drop (eqn (7)) and an unaffected electron mobility (situation *i*) are depicted in Figure 5.b. The numerical front and back *I-V* curves are similar, in contrast to the experimental *I-V* curves for which the back

13

photocurrent was found to be higher than the front one. The numerical front *I-V* curve could only be smaller than the back one when applying a significantly stronger potential drop. However, applying a stronger potential drop led to a similar transport situation as in case 1, i.e. only the first layer of particles significantly contributed to the photocurrent. Figure 5.c depicts case 2 without any potential drop with unaffected electron mobility (situation *i*). In this case, the photocurrent density reached up to 5 mA cm^{-2} at 1.23 V$_{RHE}$ and 8 mA cm^{-2} at 1.5 V$_{RHE}$ under front-side illumination. This case is expected to occur if the LTON particles were in the form of a monocrystalline pillar or if the particles were perfectly connected to an external wire (similar to the CNT network connection approach by Dilger et al.[5]). The *I-V* curves of case 2 with the two types of electron mobility drops (situation *ii*) with electron mobility of types I and II and without any potential drop are depicted in Figure 5.d. In this case, the front and back photocurrents are very similar as for case 2 with the linear potential drop and with unaffected electron mobility (Figure 5.b). Only a much stronger mobility drop could significantly reduce the front photocurrent without affecting much the back photocurrent. However, this case would effectively lead to a photocurrent as in case 1.

The numerical *I-V* curves of case 3 (first two layers of particles in *pseudo-series*) for varying inter-particle hole transfer velocities are depicted in Figure 6. The numerical *I-V* curves for varying inter-particle electron transfer velocities are depicted in the Supporting Information, Figure S1. The inter-particle potential barrier was fixed to 0.0762 V to ensure flatband condition at the inter-particle contact, allowing the presence of electrons and holes at the inter-particle contacts. The contributions of the second particle below 0.8 V$_{RHE}$ were not relevant since the onset potential is at ~0.8 V$_{RHE}$, as visible in Figure 6.a and b. As depicted in Figure 6, the contribution of the second particle reached up to 59 % under front-side illumination and up to 48 % under back-side illumination. Indeed, the integrated generation rate in the second particle was higher than in the first particle under front-side illumination but the situation was inverted under back-illumination with a higher integrated generation rate in the first particle. The smaller the inter-particle velocity, the smaller the contribution of the second particle at higher potential because fewer holes in the first particle are available to recombine with electrons of the second particle. The numerical *I-V* curves were only within the experimental variation when the contribution of the second particle was below 10 % at 1.23 V$_{RHE}$ under back-side illumination and below 5 % under front-side illumination for a numerical photocurrent within the experimental errors bars from 0.94 V$_{RHE}$ to 1.5 V$_{RHE}$, i.e. the inter-particle hole velocity was below or equal to 10^{-4} m s^{-1}. In other words, this inter-particle charge transfer mechanism provided numerical *I-V* curves similar to the experimental ones only when the contribution of the second particle was minor (<20 %). Moreover, it is unlikely that the potential barrier at the inter-particle is negligible in order to allow for the presence of holes in the first particle and electrons in the second particle. A significant potential barrier would reduce even further the chance of having this inter-particle charge transfer mechanism occurring. This observation also supports our observation that inter-particle charge transfer does not play a major role in our LTON PBPEs and that only particles in direct contact with the FTO are significantly contributing to the photocurrent (case 1).
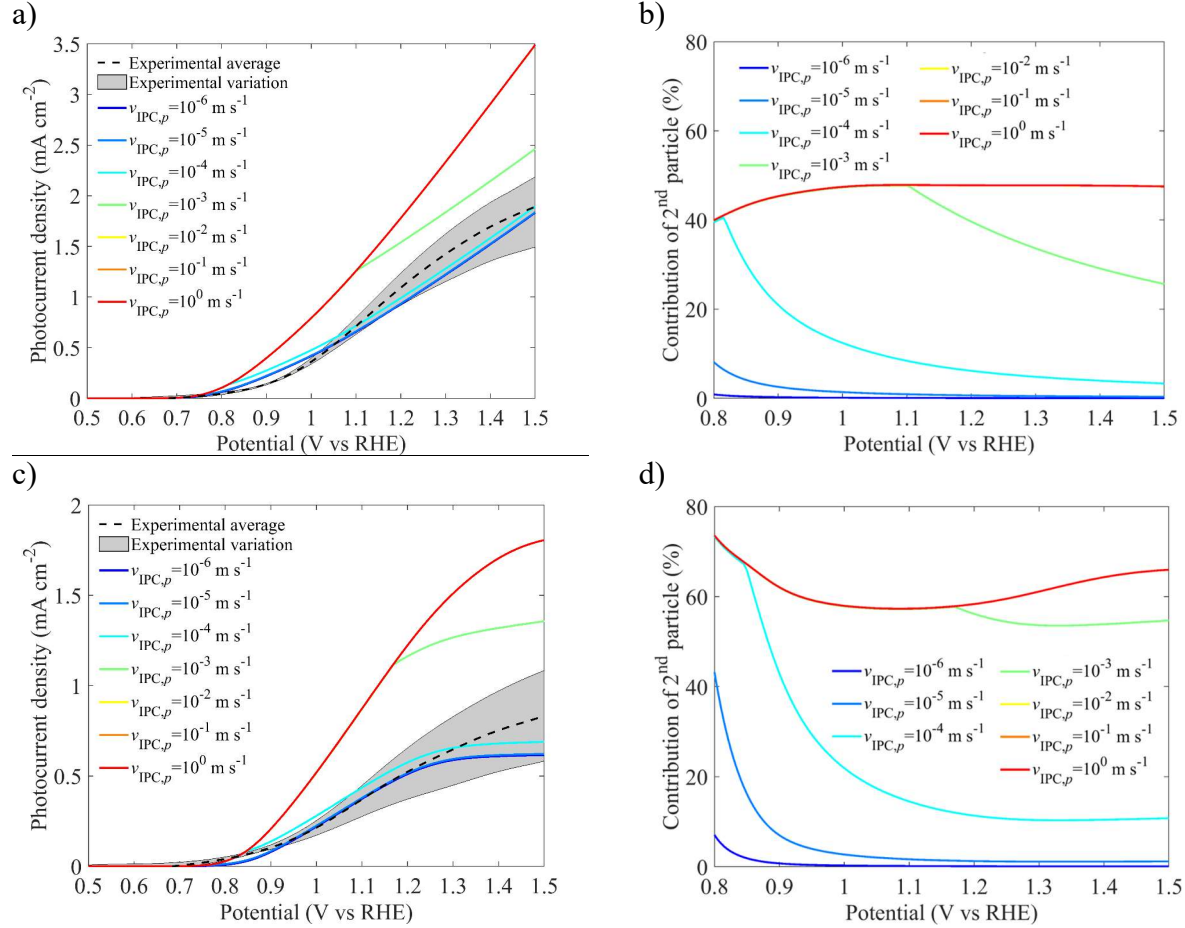
Figure 6. Experimental *I-V* curves of best-LTON PBPE with an average film thickness of 8.43 µm taken from Gaudy et al.[13]. The corresponding numerical *I-V* curves of case 3 for varying inter-particle hole transfer velocities under a) back-side illumination and c) front-side illumination, and the corresponding contribution of the 2nd particle on the right side in b) and d).

3.3. Impact of Particle Size on the Photocurrent

In literature, mainly two particle sizes have been studied experimentally: the particles of bare-LTON, SS-LTON (see section 2.4), with sizes in the range of 1.79 and 0.27 µm (longest direction and shortest direction of rectangular particles) [16] and the particle synthesized by polymerized-complex reaction (PC-LTON) with a size of 50 to 300 nm (roughly spherically shaped particles)[6,28]. The PBPE made of the smaller size PC-LTON particles led to a photocurrent density much smaller, 0.06 mA cm^{-2} at 1.8 V_{RHE}, than the one of the PBPEs made of the larger SS-LTON particles, 2.34 mA cm^{-2} at 1.8 V_{RHE}[6]. The particle must be of a certain size to see a fully developed band bending such as verified by open circuit measurements for SS-LTON[13], which could explain at a first glance the poor performance of smaller PC-LTON PBPEs. However, the doping concentration in LTON is $7 \cdot 10^{17}$ cm^{-3} and the permittivity is 15, which induces a SCR of few nanometers only[13]. The PC-LTON particles are around 50-300 nm[6,28], a size sufficient to have a fully developed band bending at the SC-EL interface. Thus, the poor performance of PC-LTON PBPE cannot be attributed to the absence of a bend bending at the SC-EL interface.

Feng et al. [6] attributed the poor performance of PC-LTON PBPE to insufficient penetration of TiCl$_4$ necking agent. However, our nano-tomography study of the LTON PBPEs[16] indicated that the necking was uniformly distributed within the electrode and present at almost all inter-particle locations. Thus, it seems that the limited contribution of particles not in direct contact with FTO is more likely the reason for the worse performance of PC-LTON PBPE. Indeed, the smaller the size of the particle is, the less light is absorbed in the first particle layer and the smaller is the resulting photocurrent. We computed the generation rate and the photogenerated current density of PC-LTON and SS-LTON PBPEs to support our hypothesis by using the same EMW propagation model than Gaudy et al.[13]. The same solid phase density profile and optical properties[13] were assumed for PC-LTON and for SS-LTON. A total film thickness of 8.43 µm was assumed for both types of LTON and a first particle thickness of 200 nm was assumed for PC-LTON and 1.42 µm for SS-LTON. As depicted in Figure 7, the back photogenerated current density of PC-LTON was ten times smaller than the one for SS-LTON. This result is in accordance with the work of Feng et al.[6] in which they observed a constant increase of the photocurrent with the size of the particles.
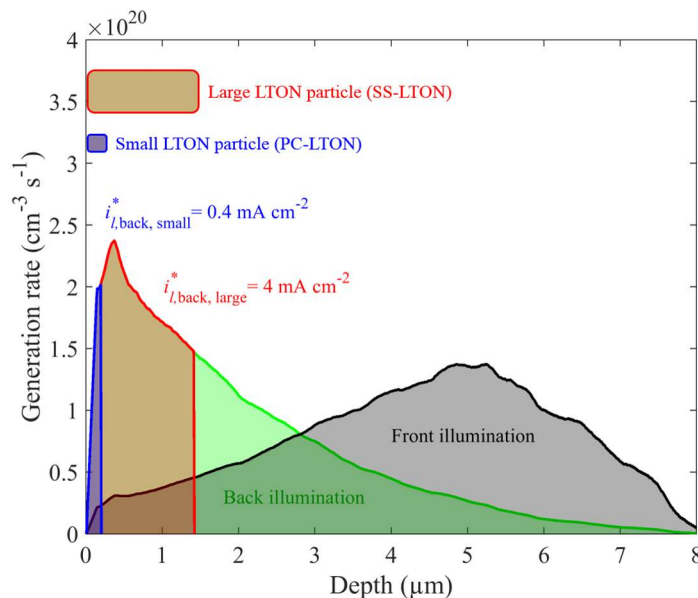

Figure 7. Generation rate and photogenerated current density under back-side illumination for small LTON (PC-LTON) and large LTON (SS-LTON) PBPEs.

Moreover, Feng et al. observed that PBPEs made of multiple layers of smaller particles (LTON PC 1000) led to higher back than front photocurrent, while PBPEs made of a single layer of larger particles (LTON SSR 1250) led to similar front and back photocurrent. This observation suggests that additional layers only reduce the radiation arriving at the first layer of particles, leading to a lower front than back photocurrent. In contrast, the PBPEs made of larger particles are composed of one or, maximally, two layers of particles, reducing less the light arriving at the particles in direct contact with the FTO for front-side illumination[32].

By explaining higher photocurrents by better inter-particle contacts through necking[4,6,7] and neglecting the likely minor contribution of charge carriers from particles away from the FTO, the community might have focused on increasing the inter-particle conductivity rather than improved contacts between the FTO and the first layer of particles. Based on our modeling results, we hypothesize that the central effect of necking consists in increasing the conductivity between the first layer of particles and the FTO.

3.4. Design Guidelines for Particle-Based Photoelectrodes

We hypothesize that there is a hole quasi-Fermi level discontinuity (Figure 1.d) between particles with inter-particle necking since the contact area between particles is only of few square nanometers. This small inter-particle area, typical for our electrodeposited particle-based LTON photoelectrodes, is in contrast to the large inter-grain area present in vapor phase deposited cauliflower hematite photoelectrodes[24,33], in which the surface of each nanostructured grain is smooth and fully in contact with other grains. Moreover, the presence of interfacial states between particles is likely to create a double Schottky junction between particles, similar to what has been observed in polycrystalline silicon with a potential barrier that hinders the transfer of electrons between particles[20,21]. Indeed, the necking treatment of these LTON photoelectrodes were done at a temperature of 643 K[3]. This temperature might be too low to enable inter-diffusion of atoms between particles and thus cannot mitigate the Schottky barrier. Whereas the contact between the FTO and the first layer of particles allows the transfer of electrons thanks to the TiO_2 necking as discussed in section 2.2. Connecting particles by necking, however, remains very challenging and has not been successfully achieved even with TiO_2 as the best necking material[3]. Simpler approaches could be undertaken to improve the efficiency of PBPEs since mostly the first layer of particles is contributing to the photocurrent. We predict an efficiency improve of PBPEs by increasing the solid phase density of the first layer of particle, currently being only 0.28. Indeed, a single layer of particles with a solid phase density close to 1 and with electrolyte-connected nano-pores to maintain a large surface area would be enough to absorb all the incoming light based on the complex refractive index of LTON[13]. This was achieved by Akiyama et al.[34] by a single particle layered PBPE, where the particles were etched to enhance the internal network of nano-pores of LTON particles, obtaining a photocurrent density increase of a factor of 7.4, i.e. 1.2 mA cm^{-2} here compared to 8.9 mA cm^{-2} in the work of Akiyama et al. at 1.23 V_{RHE}. The active surface area of the PBPEs was increased by creating nano-pores [34] but, more importantly, by doing so the path of holes generated inside the particle was significantly reduced due to additional nano-pores in contact with the electrolyte enabling the potential for high performing PBPEs. In contrast, thin LTON films without an enhanced diffusion length showed only poor performance[35]. In Akiyama et al., the electrons were extracted by depositing Ti on the LTON particles, in contrast to here, where TiO_2 necking was used. But also for the LTON-Ti contact, a built-in field promotes the electron transfer since the conduction band of LTON is at -4.2±0.1 V_{vac}[17], well aligned with the one of Ti at -4.3 V_{vac}[36]. Thus, the electrons can transfer also efficiently from the LTON particles to the Ti conductive substrate. The use of a metal foil as a back contact can also improve the contact between the particles and the conductive substrate, enabling an increased annealing temperature compared to using an FTO as conductive substrate.
Adding a conductive network, as in the work of Dilger et al.[5], radically changes the mechanism of the majority charge carrier transport since the inter-particle charge transfer is replaced by external "wires" that transport the majority charge carriers from the particle directly to the FTO substrate.

Therefore, upper particles can also contribute to the photocurrent (Figure 8.b) and the front photocurrent can be higher than the back one. Adding a conductive network will decrease the surface area of the particle in contact with the electrolyte, and while we do not expect the particle surface coverage by the conductive network to be large, the network's size and shape should be optimized to maximize the particle's active area in contact with the electrolyte, while maintaining a sufficiently large area to facilitate high electron transfer from the particle to the network. Co-catalysts already work efficiently even if the coverage is not very large[3]. In addition, the conductive network should not be redox active to avoid backward reactions (lower shunt resistance and higher dark current). Thus ideally, the conductive network should be redox inactive and composed of fibers or nanowires oriented perpendicularly to the FTO surface (to minimize the parasitic light absorption by the conductive network) while connecting all particles with the FTO substrate (Figure 8).
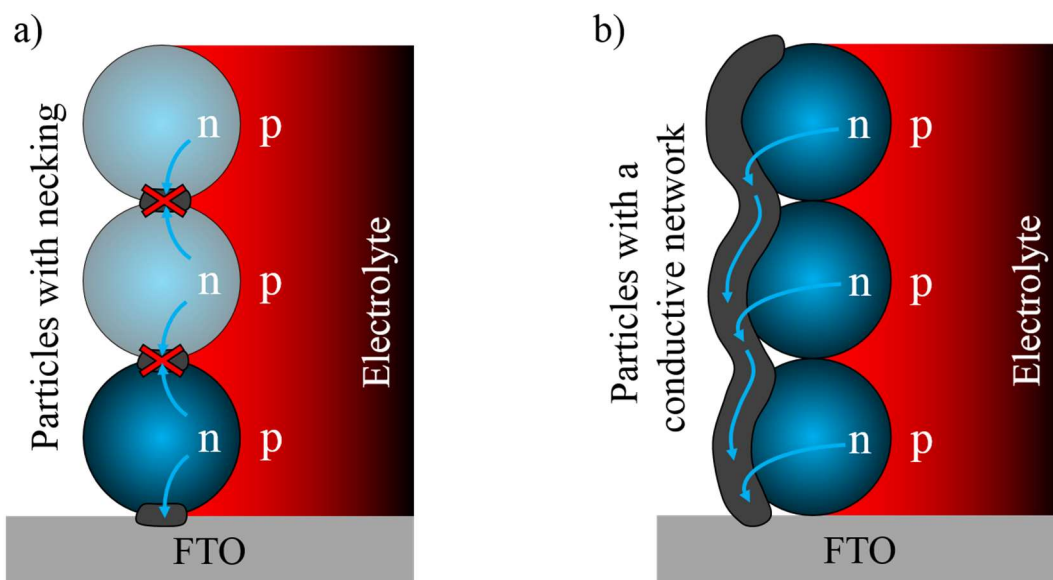

Figure 8. Schemes of particulate photoabsorber water-splitting systems: a) PBPE with inter-particle contacts and b) PBPE with a conductive network.

Having a conductive network will result in similar charge transport situation as our modeling case 2, considering a potential drop depending on the effectiveness of the network conductivity. For a perfectly conductive network, the photocurrent density in LTON PBPEs can reach 5 mA cm^{-2} at 1.23 V_{RHE}, i.e. a photocurrent density increase of 3.8 mA cm^{-2} at 1.23 V_{RHE} (Figure 5.c).

The photocurrent can even be further increased by improving the water oxidation reaction kinetics, as predicted by simulations[13]. We carried out experiments and deposited 50 nm layer IrO$_x$ (Figure S2 in the Supporting Information)—one of the best oxygen evolution cocatalyst[37]—onto our PBPEs. We found strongly increased photocurrents, i.e. a relative increase of 67 % at 1.23 V_{RHE} (section S2 in the Supporting Information). However, IrO$_x$ might not only improve the reaction kinetics but potentially connect upper particles with the FTO glass substrate since IrO$_x$ can exhibit high conductivity (in the range of 2.56×10^6 S m^{-1}[38]). However, adding a 50 nm layer of IrO$_x$ did not allow measuring front to back photocurrent ratios since the IrO$_x$ completely blocks the light under front-side illumination. Therefore, we were unable to determine if the deposition of a 50 nm layer IrO$_x$ contributes to connect upper particles with the FTO glass substrate. Nevertheless, the

deposition of a layer of conductive transparent co-catalyst over all the particles might be an interesting approach to connect upper particles with the FTO glass substrate, similarly to CNT while improving the oxygen evolution reaction kinetic.

4.   Conclusion

We investigated the inter-particle charge transfer in particle-based photoelectrodes (PBPEs) using LTON particles as model system. Based on the new understanding of this charge transfer, we provided mesostructural guidelines for high performing PBPEs.

Experimental measurements of the thickness-dependence of the front and back photocurrent were undertaken to provide qualitative information about majority charge carrier transport limitation. A simple numerical model, allowing to calculate front to back photogenerated current ratios, was developed and compared to the experimental front to back photocurrent ratio. The results suggested that only a limited part of the overall PBPE thickness contributed to the photocurrent. The best fit between the experimental and the numerical front to back current ratio was obtained for a contributing thickness of 450 nm with a solid phase density of 0.28. Different possible inter-particle charge transfer mechanisms were then described and implemented in a more advanced 2D multi-physics PBPE model. The numerical I-V curves were predicted and subsequently compared to experimental I-V curves. The results showed that matching was obtained only when the first layer of particles in direct contact with the FTO dominated the photocurrent, i.e. the inter-particle contact can be approximated by a double Schottky barrier too high to allow any electron transfer. We also showed that considering an ohmic contact between particles with a high resistance—a large inter-particle potential drop—could fit reasonably well experimental I-V curves. If considering only a small inter-particle resistance, the numerical front photocurrent was higher than the back photocurrent, contradicting the experimentally measured photocurrents. Moreover, the numerical front photocurrent was 5 mA cm^{-2} when assuming no inter-particle resistance, much higher than the experimental front photocurrent that lied within 0.4 to 0.7 mA cm^{-2}. Similarly, a low inter-particle resistivity with a low inter-particle electron mobility resulted in a good match between numerical and measured I-V curves. Considering two particles in pseudo-series, the numerical front photocurrent was within the experimental error bars (from 0.94 V_{RHE} to 1.5 V_{RHE}) but only when the photocurrent contribution of the second particle was below 5 %. Thus, these alternatives (ohmic contact with large inter-particle resistance, or pseudo-series with low inter-particle charge carrier velocities) predicted insignificant inter-particle transport and therefore also that only the first layer of particles significantly contributed to the photocurrent.

The impact of particle size of the PBPE on the photocurrent performance and on the front to back photocurrent ratio was investigated based on published experimental studies with different LTON particle sizes. The photoelectrodes with smaller particles (50 to 300 nm) provided a significantly smaller photocurrent density (0.06 mA cm^{-2} at 1.8 V_{RHE}) than the ones with large particles (1.79 and 0.27 μm, photocurrent of 2.34 mA cm^{-2} at 1.8 V_{RHE})[6]. The back photocurrent was higher than the front photocurrent for photoelectrodes with multiple layer of small particles while for 1-2 layers of larger particles the back and front photocurrent was similar[6]. These observations further supported that only the first layer of particles in direct contact with the FTO glass substrate significantly contributes to the photocurrent.

We recommend that experimental approaches for necking or conductive network design in PBPE focus on particle-substrate connection and not on inter-particle connection. Inter-particle mobility and/or charge carrier velocity would need improvements of multiple orders of magnitude. On the other hand, adding a conductive network to connect the LTON particles to the FTO glass substrate

could-according to our model-improve the photocurrent density from 1.2 mA cm^{-2} to 5 mA cm^{-2} at 1.23 V$_{RHE}$ under front-side illumination. Generally, attention should be put on the first layer of particles and increasing the solid phase density of this layer in direct contact with the FTO glass substrate should be prioritized. New conductive network designs with different conductive materials to connect particles directly with the FTO should be developed such as the deposition of a transparent co-catalyst layer over all particles joining the function of a cocatalyst and a conductive network. Using co-catalysts transparent to the visible light would allow measuring front-side illumination and front to back photocurrent ratios. Furthermore, the influence of the co-catalyst layer thickness on the performance under front- and back-side illumination could determine if this layer only improves the reaction kinetic or actually provides a conductive network to connect upper particles to the FTO glass substrate.

Author Information

Corresponding Author
Email: sophia.haussener@epfl.ch.

Notes
There are no conflicts of interest to declare.

Supporting Information

Numerical inter-particle charge transfer mechanisms for varying inter-particle electron transfer velocities and best-LTON photoelectrodes with 50 nm IrO$_x$.

Acknowledgments

References

(1) Fountaine, K. T.; Lewerenz, H. J.; Atwater, H. A. Efficiency Limits for Photoelectrochemical. *Nat. Commun.* **2016**, *7*, 1–9.

(2) Pinaud, B. a.; Benck, J. D.; Seitz, L. C.; Forman, A. J.; Chen, Z.; Deutsch, T. G.; James, B. D.; Baum, K. N.; Baum, G. N.; Ardo, S.; et al. Technical and Economic Feasibility of Centralized Facilities for Solar Hydrogen Production via Photocatalysis and Photoelectrochemistry. *Energy Environ. Sci.* **2013**, *6*, 1983–2002.

(3) Landsmann, S.; Maegli, A. E.; Trottmann, M.; Battaglia, C.; Weidenkaff, A.; Pokrant, S. Design Guidelines for High-Performance Particle-Based Photoanodes for Water Splitting: Lanthanum Titanium Oxynitride as a Model. *ChemSusChem* **2015**, *8*, 3451–3458.

(4) Nishimura, N.; Raphael, B.; Maeda, K.; Le Gendre, L.; Abe, R.; Kubota, J.; Domen, K. Effect of TiCl$_4$ Treatment on the Photoelectrochemical Properties of LaTiO$_2$N Electrodes for Water Splitting under Visible Light. *Thin Solid Films* **2010**, *518*, 5855–5859.

(5) Dilger, S.; Landsmann, S.; Trottmann, M.; Pokrant, S. Carbon Containing Conductive

Networks in Composite Particle-Based Photoanodes for Solar Water Splitting. *J. Mater. Chem. A* **2016**, *4*, 17087–17095.

(6)   Feng, J.; Luo, W.; Fang, T.; Lv, H.; Wang, Z.; Gao, J.; Liu, W.; Yu, T.; Li, Z.; Zou, Z. Highly Photo-Responsive LaTiO2N Photoanodes by Improvement of Charge Carrier Transport among Film Particles. *Adv. Funct. Mater.* **2014**, *24*, 3535–3542.

(7)   Higashi, M.; Domen, K.; Abe, R. Fabrication of Efficient TaON and Ta3N5 Photoanodes for Water Splitting under Visible Light Irradiation. *Energy Environ. Sci.* **2011**, *4*, 4138–4147.

(8)   van de Krol, R.; Grätzel, M. *Photoelectrochemical Hydrogen Production*; van de Krol, R., Grätzel, M., Eds.; Electronic Materials: Science & Technology; Springer: Boston, 2012.

(9)   Jeng, M.-J.; Wung, Y.-L.; Chang, L.-B.; Chow, L. Particle Size Effects of TiO2 Layers on the Solar Efficiency of Dye-Sensitized Solar Cells. *Int. J. Photoenergy* **2013**, *2013*, 1–9.

(10)   Bisquert, J.; Marcus, R. A. Device Modeling of Dye-Sensitized Solar Cells. In *Multiscale Modelling of Organic and Hybrid Photovoltaics*; Beljonne, D., Cornil, J., Eds.; Berlin, 2013; pp 325–396.

(11)   Bisquert, J. Theory of the Impedance of Charge Transfer via Surface States in Dye-Sensitized Solar Cells. *J. Electroanal. Chem.* **2010**, *646*, 43–51.

(12)   Peter, L. M. Dye-Sensitized Nanocrystalline Solar Cells. *Phys. Chem. Chem. Phys.* **2007**, *9*, 2630–2642.

(13)   Gaudy, Y. K.; Dilger, S.; Landsmann, S.; Aschauer, U.; Pokrant, S.; Haussener, S. Determination and Optimization of Material Parameters of Particle-Based LaTiO2N Photoelectrodes. *J. Mater. Chem. A* **2018**, *6*, 17337–17352.

(14)   Dotan, H.; Sivula, K.; Grätzel, M.; Rothschild, A.; Warren, S. C. Probing the Photoelectrochemical Properties of Hematite (α-Fe2O3) Electrodes Using Hydrogen Peroxide as a Hole Scavenger. *Energy Environ. Sci.* **2011**, *4*, 958–964.

(15)   Bedoya Lora, F. E.; Hankin, A.; Kelsall, G. H. En Route to a Unified Model for Photo-Electrochemical Reactor Optimization. I - Photocurrent and H2 Yield Predictions. *J. Mater. Chem. A* **2017**, No. 16 mm, 22683–22696.

(16)   Suter, S.; Cantoni, M.; Gaudy, Y. K.; Pokrant, S.; Haussener, S. Linking Morphology and Multi-Physical Transport in Structured Photoelectrodes. *Sustain. Energy Fuels* **2018**, *2*, 2661–2673.

(17)   Paven-Thivet, C. Le; Ishikawa, A.; Ziani, A.; Gendre, L. Le; Yoshida, M.; Kubota, J.; Tessier, F.; Domen, K. Photoelectrochemical Properties of Crystalline Perovskite Lanthanum Titanium Oxynitride Films under Visible Light. *J. Phys. Chem. C* **2009**, *113*, 6156–6162.

(18)   Scanlon, D. O.; Dunnill, C. W.; Buckeridge, J.; Shevlin, S. A.; Logsdail, A. J.; Woodley, S. M.; Catlow, C. R. A.; Powell, M. J.; Palgrave, R. G.; Parkin, I. P.; et al. Band Alignment of Rutile and Anatase TiO2. *Nat. Mater.* **2013**, *12*, 798–801.

(19)   Rühle, S.; Cahen, D. Electron Tunneling at the TiO2/Substrate Interface Can Determine Dye-Sensitized Solar Cell Performance. *J. Phys. Chem. B* **2004**, *108*, 17946–17951.

(20)   Blatter, G.; Greuter, F. Carrier Transport through Grain Boundaries in Semiconductors. *Phys. Rev. B* **1986**, *33*, 3952–3966.

(21)   Greuter, F.; Blatter, G. Electrical Properties of Grain Boundaries in Polycrystalline Compound Semiconductors. *Semicond. Sci. Technol.* **1990**, *5*, 111–137.

(22)   Goetzberger, A.; Hebling, C.; Schock, H.-W. Photovoltaic Materials, History, Status and Outlook. *Mater. Sci. Eng. R* **2003**, *40*, 1–46.

(23)   Lan, C. W.; Lan, A.; Yang, C. F.; Hsu, H. P.; Yang, M.; Yu, A.; Hsu, B.; Hsu, W. C.; Yang,

A. The Emergence of High-Performance Multi-Crystalline Silicon in Photovoltaics. *J. Cryst. Growth* **2017**, *468*, 17–23.

(24)   Warren, S. C.; Voïtchovsky, K.; Dotan, H.; Leroy, C. M.; Cornuz, M.; Stellacci, F.; Hébert, C.; Rothschild, A.; Grätzel, M. Identifying Champion Nanostructures for Solar Water-Splitting. *Nat. Mater.* **2013**, *12*, 842–849.

(25)   Gaudy, Y. K.; Haussener, S. Utilizing Modeling, Experiments, and Statistics for the Analysis of Water-Splitting Photoelectrodes. *J. Mater. Chem. A* **2016**, *4*, 3100–3114.

(26)   Levinson, J.; Shepherd, F. R.; Scanlon, P. J.; Westwood, W. D.; Este, G.; Rider, M. Conductivity Behavior in Polycrystalline Semiconductor Thin Film Transistors. *J. Appl. Phys.* **1982**, *53*, 1193–1202.

(27)   Verlaak, S.; Arkhipov, V.; Heremans, P. Modeling of Transport in Polycrystalline Organic Semiconductor Films. *Appl. Phys. Lett.* **2003**, *82*, 745–747.

(28)   Maegli, A. E.; Pokrant, S.; Hisatomi, T.; Trottmann, M.; Domen, K.; Weidenka, A. Enhancement of Photocatalytic Water Oxidation by the Morphological Control of LaTiO2N and Cobalt Oxide Catalysts. *J. Phys. Chem. C* **2014**, *118*, 16344–16351.

(29)   Landsmann, S.; Surace, Y.; Trottmann, M.; Dilger, S.; Weidenka, A.; Pokrant, S. Controlled Design of Functional Nano-Coatings: Reduction of Loss Mechanisms in Photoelectrochemical Water Splitting. *ACS Appl. Mater. Interfaces* **2016**, *8*, 12149–12157.

(30)   Niu, W.; Moehl, T.; Cui, W.; Wick-Joliat, R.; Zhu, L.; Tilley, S. D. Extended Light Harvesting with Dual Cu2O-Based Photocathodes for High Efficiency Water Splitting. *Adv. Energy Mater.* **2018**, *8*, 1–8.

(31)   Xiao, S.; Chen, H.; Yang, Z.; Long, X.; Wang, Z.; Zhu, Z.; Qu, Y.; Yang, S. Origin of the Different Photoelectrochemical Performance of Mesoporous BiVO4 Photoanodes between the BiVO4 and the FTO Side Illumination. *J. Phys. Chem. C* **2015**, *4*, 151004165821008.

(32)   Minegishi, T.; Nishimura, N.; Kubota, J.; Domen, K. Photoelectrochemical Properties of LaTiO2N Electrodes Prepared by Particle Transfer for Sunlight-Driven Water Splitting. *Chem. Sci.* **2013**, *4*, 1120–1124.

(33)   Cesar, I.; Sivula, K.; Kay, A.; Zboril, R.; Grätzel, M. Influence of Feature Size, Film Thickness, and Silicon Doping on the Performance of Nanostructured Hematite Photoanodes for Solar Water Splitting. *J. Phys. Chem. C* **2009**, *113*, 772–782.

(34)   Akiyama, S.; Nakabayashi, M.; Shibata, N.; Minegishi, T.; Asakura, Y.; Abdulla-Al-Mamun, M.; Hisatomi, T.; Nishiyama, H.; Katayama, M.; Yamada, T.; et al. Highly Efficient Water Oxidation Photoanode Made of Surface Modified LaTiO2N Particles. *Small* **2016**, *12*, 5468–5476.

(35)   Pichler, M.; Si, W.; Haydous, F.; Téllez, H.; Druce, J.; Fabbri, E.; Kazzi, M. El; Döbeli, M.; Ninova, S.; Aschauer, U.; et al. LaTiOxNy Thin Film Model Systems for Photocatalytic Water Splitting: Physicochemical Evolution of the Solid–Liquid Interface and the Role of the Crystallographic Orientation. *Adv. Funct. Mater.* **2017**, *27*, 1–18.

(36)   Lide, D. R. CRC Handbook of Chemistry and Physics. *J. Am. Chem. Soc.* **2005**, 1–2661.

(37)   McCrory, C. C. L.; Jung, S.; Peters, J. C.; Jaramillo, T. F. Benchmarking Heterogeneous Electrocatalysts for the Oxygen Evolution Reaction. *J. Am. Chem. Soc.* **2013**, *135*, 16977–16987.

(38)   El Khakani, M. A.; Chaker, M.; Gat, E. Pulsed Laser Deposition of Highly Conductive Iridium Oxide Thin Films. *Appl. Phys. Lett.* **1996**, *69*, 2027–2029.
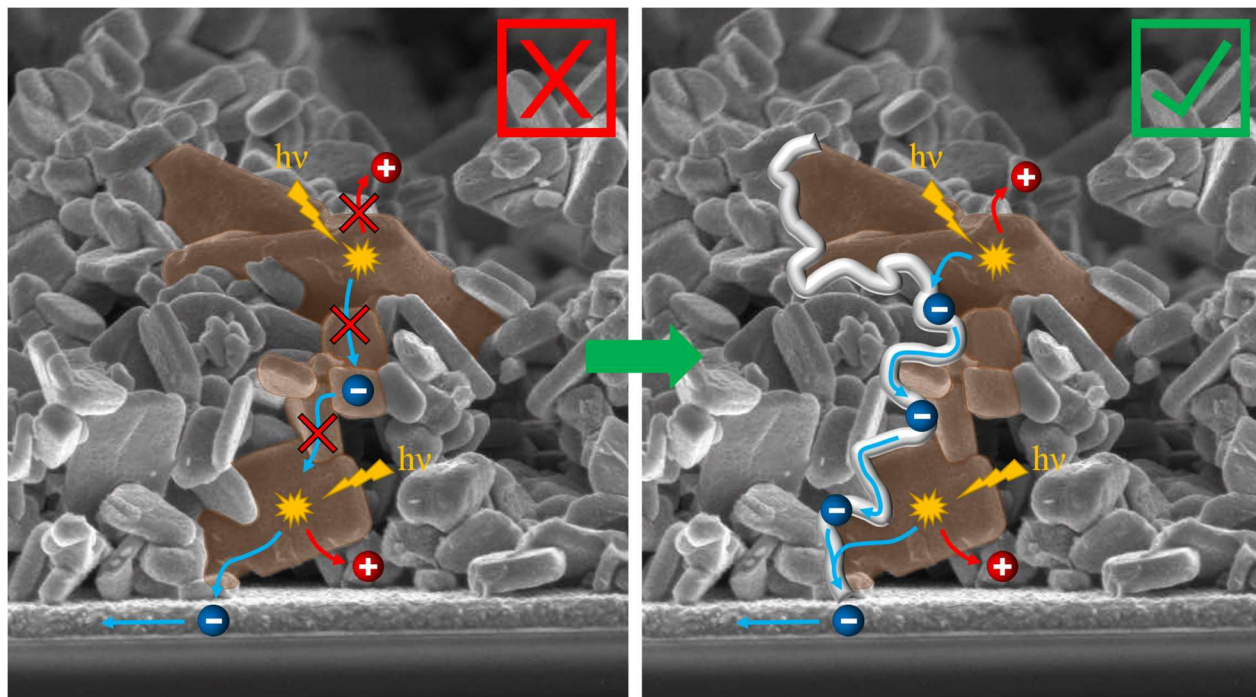
TOC Figure (9.2x16.2cm for conversion to 8.5x4.75 cm, 1771x981 pixels)